

Slave-boson phase diagram of the two-dimensional extended Hubbard model: influence of electron-phonon coupling

M. Deeg, H. Fehske, H. Büttner

Physikalisches Institut, Universität Bayreuth, W-8580 Bayreuth, Germany

Received: 21 October 1992

Abstract. We present a detailed study of the extended Hubbard-Peierls model on a square lattice using the slave-boson method proposed by Kotliar and Ruckenstein. The emphasis is on the investigation of the ground state phase diagram. To compare the relative stability of several homogenous phases, the effective bosonized action was evaluated by means of a two-sublattice saddle-point approximation which allows for the symmetry broken states compatible with the underlying bipartite lattice structure. Paying particular attention to the interplay of electron-electron and electron-phonon interaction, we take into account various types of magnetic ordered phases, i.e. para-, ferro-, ferri-, and antiferromagnetic states, as well as charge ordered phases, e.g. a static (π, π) Peierls distorted state. Furthermore the approach has been applied to the following special cases: the Hubbard model, the extended Hubbard model, and the Hubbard-Peierls model. A careful numerical solution of the corresponding self-consistency equations enables us to map out the ground-state phase diagrams of the various models at arbitrary band filling over the whole range of interaction strength. In the phase diagram of the Hubbard model we found a large region with ferrimagnetic order away from half-filling. The phase diagram of the half-filled band extended Hubbard model shows a first-order transition from a spin-density-wave to a charge-density-wave state which is displaced from the mean-field line $U = 4V$ towards larger V . At large negative U and V we obtain a domain with charge separation. The phase compares favorably with earlier quantum Monte-Carlo results. Including the local electron-phonon coupling the charge-density-wave region is considerably enlarged. Away from half-filling the phase diagram becomes more complex: besides the pure magnetic phases we obtain ferri- and paramagnetic states which show additional charge-density order. Aspects of phase separation are discussed. Finally we investigate the variation of the different gap and order parameters along characteristic lines in the parameter space and determine the renormalized quasiparticle bands.

I. Introduction

The considerable activity in the field of high- T_c superconductivity has aroused interest, once again, in theoretical models describing strongly correlated electrons. It is generally agreed that the simple Hubbard model (HM) contains the basic interactions to explain the main normal-state properties of these systems [1]. While most of the current work concerns the possibility of a pure electronic pairing mechanism within the framework of the two-dimensional (2D) HM [2, 3], the physical properties of the HM are also expected to be important for understanding of itinerant magnetism [4] or a description of the Mott-Hubbard metal-insulator transition [5]. For this reason, the Hubbard Hamiltonian and its variants have been extensively studied in the past few years.

In particular, the extended Hubbard model (EHM), which includes nearest-neighbour Coulomb interaction, has attracted much attention. Long range Coulomb interaction is expected to play an important role in a variety of low-dimensional materials, such as 1D conducting polymers [6] and charge transfer salts [7]. From a more theoretical point of view the incorporation of interatomic Coulomb interaction may be desirable to exclude (unphysical) phase separated states which has been discussed recently for the pure HM and the related $t - J$ model [8]. In one spatial dimension the half-filled EHM has been investigated using, among other techniques, renormalisation-group methods [9, 10], exact Lanczos-diagonalisation [11–13] and Monte-Carlo simulation [14, 15]. The ground state phase diagram of the EHM shows a surprising richness. For repulsive on- and intersite Coulomb interactions ($U, V > 0$) the ground state of the system can be a spin-density-wave (SDW) with continuous symmetry or a truly long-range ordered charge-density-wave phase (CDW). Monte-Carlo [15] and Lanczos results [12, 16] indicate that the SDW-CDW transition occurs slightly above the $U = 2V$ line given by renormalisation group [10, 17] and Hartree-Fock [18] calculations. A quantum Monte-Carlo simulation of the 2D EHM shows that the 1D and 2D cases are qualitatively similar, where the SDW-CDW transition is found for the square lattice near the

line $U=4V$ [19]. The EHM with on-site and/or intersite attractive interaction has been intensively studied as a theoretical model of local electron pairing in the context of superconductivity (for an overview see Micnas et al. [20]). The negative- U Hubbard model describes the crossover from a BCS-like superconductivity to the superfluidity of charged bosons. In the strong-attraction limit one observes preformed local pairs (bipolarons). The interatomic Coulomb interaction will stabilize CDW ordering ($V>0$) or singlet (on-site) superconductivity ($V<0$). The negative- V EHM ($U>0$) is expected to lead to anisotropic superconducting states for weak on-site correlations and to a SDW phase in the strong-coupling U -limit (cf. [20], and references therein). At large negative V , a first-order transition to a charge separated state is found by Monte-Carlo [15] and Lanczos [12] technique. A physical mechanism leading to such a type of effective short-range electron-electron attraction can be, among others, a strong local electron-phonon coupling [20–22].

Obviously, the interplay of electron-electron and electron-phonon coupling in highly correlated Fermi systems is of special importance for an understanding of both superconducting and normal state properties of e.g. the high- T_c oxide systems. To discuss this question from a microscopic point of view, the incorporation of electron-phonon interaction is frequently based on a local Holstein (Peierls) coupling to the electronic system [23–32]. Thus, the physics of the resulting model is governed by three competing effects: the itinerancy of the electrons, their Coulomb interaction and the electron-phonon coupling. The equilibrium state of the system will depend on the relative strengths of electron-electron and electron-phonon interaction as well as on the ratio of phonon frequency to the renormalised bandwidth, i.e. on the adiabatic or nonadiabatic nature of the coupling [22]. The nonadiabatic strong coupling case may lead to polaron formation, where the polaronic band-narrowing favours the strong correlation limit [31]. Along this line polaronic or bipolaronic theories of superconductivity have been developed [24, 33]. In the opposite adiabatic limit a CDW (bipolaronic) insulator with frozen local lattice distortions may be formed [34].

Motivated by this situation the purpose of our paper is the investigation of the ground state properties of the 2D EHM with (and without) additional onsite electron-phonon coupling, i.e. the so-called extended Hubbard-Peierls model (EHPM). The stability of the 2D Hubbard-Peierls model (HPM) against a static Peierls distortion was studied using Hartree-Fock [24] and Monte-Carlo methods [25]. In previous work [29, 30] we have obtained first results for the phase diagram of the HPM using the slave-boson (SB) scheme introduced by Kotliar and Ruckenstein [35]. Their auxiliary boson approach can be readily generalized by the incorporation of electron-phonon coupling [30, 36]. For the HM, Lilly et al. [37] have performed a comparative study of the SB mean-field approach [35] and quantum Monte-Carlo calculations, where an excellent agreement was obtained for groundstate energy and several local quantities. In addition the SB representation [35] provides a symmetric representation of spin and charge excitations [54]. Therefore, the SB

formalism [35] should be a reasonable starting point for a theoretical treatment of the EHPM as well.

This article is organized as follows. In Sect. II we discuss the model and sketch briefly the slave boson approximation scheme. Section III is devoted to the numerical evaluation of the resulting saddle-point equations. We analyse various types of spin and charge order and present an extensive investigation of the ground-state phase diagram of the EHM and the EHPM in Sect. IIIA and Sect. IIIB, respectively. The issue of phase separation is discussed. In Sect. IIIC we determine the corresponding phase diagrams of the HM and HPM in the whole range of parameters. Finally, in Sect. IV we summarize the main results of our work.

II. Two-sublattice slave boson approach

Let us first discuss our model. The single-band extended Peierls-Hubbard model is given by the Hamiltonian:

$$\mathcal{H} = \mathcal{H}_{\text{el}} + \mathcal{H}_{\text{el-ph}} + \mathcal{H}_{\text{ph}}, \quad (1)$$

where

$$\begin{aligned} \mathcal{H}_{\text{el}} = & -t \sum_{\langle ij \rangle, \sigma} (c_{i\sigma}^\dagger c_{j\sigma} + \text{H.c.}) \\ & + U \sum_i n_{i\uparrow} n_{i\downarrow} + V \sum_{\langle ij \rangle} n_i n_j, \end{aligned} \quad (2)$$

$$\mathcal{H}_{\text{el-ph}} = -\alpha \sum_i q_i n_i, \quad (3)$$

$$\mathcal{H}_{\text{ph}} = K \sum_{i_x, i_y} q_{i_x, i_y}^2, \quad (4)$$

describes the electron, electron-phonon, and phonon (lattice) parts respectively. Above, $c_{i\sigma}^\dagger$ and $c_{i\sigma}$ denote the creation and annihilation operators for spin σ electrons at Wannier site i , $n_{i\sigma} = c_{i\sigma}^\dagger c_{i\sigma}$ is the occupation number operator, and $n_i = n_{i\uparrow} + n_{i\downarrow}$. \mathcal{H}_{el} represents the standard extended Hubbard model, where t is the nearest neighbour (NN) hopping integral, and $\langle ij \rangle$ indicates a sum over NN pairs on a square lattice. In \mathcal{H}_{el} the first two terms together define the simple Hubbard model with an on-site electron interaction U . V measures the Coulomb interaction between electrons on NN sites. The electron-phonon interaction term $\mathcal{H}_{\text{el-ph}}$ and the elastic energy \mathcal{H}_{ph} of a harmonic lattice with spring constant K are treated within the adiabatic approximation. The electronic system is coupled locally to static lattice displacements. The Holstein coordinates q_i are conventionally interpreted as vibrational displacements of an internal optical degree of freedom of the effective lattice site i . In the context of the copper-oxide planes of, e.g., $\text{La}_{2-\delta}\text{Ba}_\delta\text{CuO}_4$ the Peierls (Holstein) coupling involves the frozen phonon displacements

$$q_{i_x, i_y} = (x_{i_x, i_y} - x_{i_x-1, i_y} + y_{i_x, i_y} - y_{i_x, i_y-1})/4 \quad (5)$$

of both oxygens in the unit cell $i=(i_x, i_y)$ along the Cu-O bond axis. This model has been frequently used to study breathing-type phonon modes [24, 25, 29]. In the

half-filled band case the electron-phonon coupling leads to the appearance of a (π, π) Peierls instability, which is connected to a staggered static distortion of the square lattice. For the (π, π) mode we have $x_{ix, iy} = -x_{ix-1, iy} = y_{ix, iy} = -y_{ix, iy-1}$ (cf. [30]); therefore, in (4) the phonon part \mathcal{H}_{ph} can be expressed as a quadratic form of the Holstein coordinates.

In order to treat the correlation effects incorporated in the EHPM in a non-perturbative way, we use the SB approach [38–40] in a formulation due to Kotliar and Ruckenstein [35]. In the spirit of [35] we introduce four auxiliary boson fields e_i^\dagger , $p_{i\sigma}^\dagger$, and d_i^\dagger which refer to the four different states of a Wannier site i , i.e., the empty one, those single occupied by an electron with spin up or down, and the doubly occupied state. In the enlarged Hilbert space of boson and fermion states these four states are expressed in terms of boson and pseudo-fermion creation operators acting on the vacuum. To enforce that only the physically relevant part of the enlarged Fock space is considered, the boson fields are enslaved to the pseudo-fermion fields $\{\tilde{c}_{i\sigma}\}$ by a set of local constraints:

$$Q_i^{(1)} = e_i^\dagger e_i + p_{i\uparrow}^\dagger p_{i\uparrow} + p_{i\downarrow}^\dagger p_{i\downarrow} + d_i^\dagger d_i - 1 = 0$$

(completeness), (6)

$$Q_{i\sigma}^{(2)} = \tilde{c}_{i\sigma}^\dagger \tilde{c}_{i\sigma} - p_{i\sigma}^\dagger p_{i\sigma} - d_i^\dagger d_i = 0$$

(one-to-one correspondence).

Substituting the original electron operator by

$$c_{i\sigma} = z_{i\sigma} \tilde{c}_{i\sigma}, \quad (7)$$

we arrive at the following SB Hamiltonian of the EHPM:

$$\begin{aligned} \mathcal{H}^{\text{SB}} = & -t \sum_{\langle ij \rangle, \sigma} (z_{i\sigma}^\dagger z_{j\sigma} \tilde{c}_{i\sigma}^\dagger \tilde{c}_{j\sigma} + \text{H.c.}) \\ & - \sum_{i, \sigma} \Delta_i \tilde{c}_{i\sigma}^\dagger \tilde{c}_{i\sigma} + \frac{1}{16\lambda} \sum_i \Delta_i^2 \\ & + U \sum_i d_i^\dagger d_i + V \sum_{\langle ij \rangle, \sigma, \sigma'} (p_{i\sigma}^\dagger p_{i\sigma} + d_i^\dagger d_i) \\ & \times (p_{j\sigma'}^\dagger p_{j\sigma'} + d_j^\dagger d_j). \end{aligned} \quad (8)$$

In the physical subspace \mathcal{H}^{SB} has the same matrix elements as the original Hamiltonian \mathcal{H} . Following [35] the operators

$$z_{i\sigma} = (1 - p_{i\sigma}^\dagger p_{i\sigma} - d_i^\dagger d_i)^{-1/2} \times (e_i^\dagger p_{i\sigma} + p_{i-\sigma}^\dagger d_i) (1 - p_{i-\sigma}^\dagger p_{i-\sigma} - e_i^\dagger e_i)^{-1/2} \quad (9)$$

and $z_{i\sigma}^\dagger$ are introduced to ensure the correct $U=0$ limit at the mean-field level. Furthermore, rescaling $\alpha q_i \rightarrow \Delta_i$ we defined in (8) the dimensionless electron-phonon coupling $\lambda = \alpha^2/16K$ (hereafter, all interaction constants (λ, U, V) and energies are measured in units of t). Note that in contrast to the HM the electronic interaction term cannot be replaced by one bilinear in the field operators. The above SB representation is manifestly not spin rotation invariant in spin space. An improved theory of Li

et al. [42] does not suffer from this shortcoming. However, we have mentioned already that even the mean-field results of the SB formalism [35] compares favorably with Monte-Carlo data [37].

The grand canonical partition function for the model (8) is given by

$$\mathcal{Z} = \text{Tr} \prod_i \delta(Q_i^{(1)}) \prod_{i, \sigma} \delta(Q_{i\sigma}^{(2)}) e^{-\beta(\mathcal{H}^{\text{SB}} - \mathcal{N}\mu)}. \quad (10)$$

Here μ is the chemical potential, and the δ -functions impose the constraints (6). Then the partition function can be expressed by a coherent state functional integral over fermion and boson fields [43]. The constraints are incorporated by a suitable integral representation of the δ -functions [44] which naturally introduces the Lagrange multipliers $\{\lambda_i^{(1)}\}$ and $\{\lambda_{i\sigma}^{(2)}\}$. Transforming the Lagrange multipliers into Bose fields, we can make use of the gauge freedom of the action (which has an $U(1)^{\otimes 3}$ gauge symmetry [30, 54, 45]) to remove three bosonic phases. After integrating out the fermionic degrees of freedom, one obtains an effective bosonic action which is an exact representation of our model (for a more detailed discussion of this point see [30]). Mean-field approximations to the functional integral are achieved by replacing the boson fields by their time averaged values [54]. At the same time the boson fields are obtained as saddle-point solutions of the free energy functional. Obviously, an unrestricted minimization of this functional is impossible for an infinite system.

At the two-sublattice mean-field level the boson fields are considered as static and uniform on each sublattice. In this case the constraints (6) can be satisfied on each sublattice only on average. The grand-canonical potential then follows as

$$\begin{aligned} \Omega = & \frac{N}{2} \sum_\eta \left\{ \lambda_\eta^{(1)} (e_\eta^2 + p_{\eta\uparrow}^2 + p_{\eta\downarrow}^2 + d_\eta^* d_\eta - 1) \right. \\ & - \sum_\sigma \lambda_{\eta\sigma}^{(2)} (p_{\eta\sigma}^2 + d_\eta^* d_\eta) + U d_\eta^* d_\eta \\ & + V \sum_{\sigma, \sigma'} (p_{\eta\sigma}^2 + d_\eta^* d_\eta) (p_{-\eta\sigma'}^2 + d_{-\eta}^* d_{-\eta}) + \frac{\Delta^2}{16\lambda} \left. \right\} \\ & + \frac{1}{\beta} \sum_{\mathbf{k}, \nu, \sigma} \ln(1 - n_{\mathbf{k}\nu\sigma}), \end{aligned} \quad (11)$$

where

$$n_{\mathbf{k}\nu\sigma} = \frac{1}{e^{\beta(E_{\mathbf{k}\nu\sigma} - \mu)} + 1} \quad (12)$$

holds, and $\eta = A, B$ denotes the sublattice index. The quasiparticle energies ($\nu = \pm 1$)

$$E_{\mathbf{k}\nu\sigma} = \lambda_\sigma^{(+)} + \varepsilon_{\mathbf{k}\nu\sigma}, \quad (13)$$

with

$$\varepsilon_{\mathbf{k}\nu\sigma} = \nu \sqrt{(\lambda_\sigma^{(-)} - \Delta)^2 + \varepsilon_{\mathbf{k}}^2 |z_{A\sigma}|^2 |z_{B\sigma}|^2}, \quad (14)$$

are obtained by diagonalising the kinetic part, where we have defined $\lambda_\sigma^{(+)} = (\lambda_{A\sigma}^{(2)} + \lambda_{B\sigma}^{(2)})/2$, $\lambda_\sigma^{(-)} = (\lambda_{A\sigma}^{(2)} - \lambda_{B\sigma}^{(2)})/2$.

$-\lambda_{B\sigma}^{(2)})/2$, and $\Delta = \Delta_A = -\Delta_B > 0$. The \mathbf{k} -summation is restricted to the magnetic Brillouin zone of the square lattice and $\varepsilon_{\mathbf{k}} = -2t(\cos k_x + \cos k_y)$ gives the unperturbed $2D$ tight-binding band structure. The free energy per site follows from (11) as

$$f = \frac{1}{N} \left(\Omega - \mu \frac{\partial \Omega}{\partial \mu} \right), \quad (15)$$

where at given electron (hole) density n ($\delta = 1 - n$), the chemical potential μ is fixed by the requirement

$$n = \frac{1}{2}(n_A + n_B) = \frac{1}{N} \sum_{\mathbf{k}, \nu, \sigma} n_{\mathbf{k}\nu\sigma}. \quad (16)$$

The sublattice particle numbers (per spin) are defined by $n_{\eta\sigma} = p_{\eta\sigma}^2 + d_{\eta}^2$. The free energy f has to be stationary with respect to variations in the bose fields e_{η} , d_{η}^* , d_{η} , $p_{\eta\sigma}$, $\lambda_{\eta}^{(1)}$, $\lambda_{\eta}^{(2)}$, and Δ . Note that the variation with respect to d_{η} and d_{η}^* yields equivalent expressions, i.e., d_{η} becomes real within the saddle-point approximation. Therefore one has to solve a set of 15 coupled self-consistency equations to get the saddle-point values of the bosonic fields. The bipartite nature of the lattice plays an essential role for the appearance of a symmetry broken state [37]. Here we are interested in a unique treatment of para-(PM), ferro-(FM), ferri-(FIM), and antiferromagnetic (AFM) long-range order, as well as of CDW ordered states. For this purpose, we introduce the following ‘order parameters’:

$$m = \frac{1}{2}(m_A + m_B) = \frac{1}{N} \sum_{\mathbf{k}, \nu, \sigma} \sigma n_{\mathbf{k}\nu\sigma}, \quad (17)$$

$$\Delta n = \frac{1}{2}(n_A - n_B) = \frac{1}{N} \sum_{\mathbf{k}, \nu, \sigma} n_{\mathbf{k}\nu\sigma} \frac{\lambda_{\sigma}^{(-)} - \Delta}{\varepsilon_{\mathbf{k}\nu\sigma}}, \quad (18)$$

$$\Delta m = \frac{1}{2}(m_A - m_B) = \frac{1}{N} \sum_{\mathbf{k}, \nu, \sigma} \sigma n_{\mathbf{k}\nu\sigma} \frac{\lambda_{\sigma}^{(-)} - \Delta}{\varepsilon_{\mathbf{k}\nu\sigma}}. \quad (19)$$

In the above equations, $m_{\eta} = n_{\eta\uparrow} - n_{\eta\downarrow}$ are the sublattice magnetisations. Then the various ordered phases can be specified as:

PM	$\Delta n = 0$	$m = 0$	$\Delta m = 0$,
PM/CDW	$\Delta n \neq 0$	$m = 0$	$\Delta m = 0$,
FM	$\Delta n = 0$	$m \neq 0$	$\Delta m = 0$,
AFM	$\Delta n = 0$	$m = 0$	$\Delta m \neq 0$,
FIM	$\Delta n \neq 0$	$m \neq 0$	$\Delta m \neq 0$ $\Delta n \simeq \Delta m$,
FIM/SDW	$\Delta n \neq 0$	$m \neq 0$	$\Delta m \neq 0$ $\Delta n \ll \Delta m$,
FIM/CDW	$\Delta n \neq 0$	$m \neq 0$	$\Delta m \neq 0$ $\Delta n \gg \Delta m$.

Eliminating the variables e_{η} , $\lambda_{\eta}^{(1)}$, and

$$p_{\eta\sigma} = \left[\frac{1}{2} \{ 1 - \delta + \xi_{\eta} \Delta n + \sigma (m + \xi_{\eta} \Delta m) \} - d_{\eta}^2 \right]^{1/2}, \quad (20)$$

the saddle-point values of m , Δn , Δm , and d_{η} are determined by an iterative solution of the remaining nonlinear stationary equations

$$U = \frac{1}{N} \sum_{\mathbf{k}, \nu, \sigma} n_{\mathbf{k}\nu\sigma} \frac{\varepsilon_{\mathbf{k}}^2 x_{\eta\sigma} x_{-\eta\sigma}^2}{\varepsilon_{\mathbf{k}\nu\sigma} y_{\eta\sigma} y_{-\eta\sigma}} \times \{ p_{\eta\uparrow}^{-1} p_{\eta\downarrow}^{-1} - [\delta - \xi_{\eta} \Delta n + d_{\eta}^2]^{-1/2} d_{\eta}^{-1} \}, \quad (21)$$

and

$$\begin{aligned} \lambda_{\eta\sigma}^{(2)} = & \frac{1}{N} \sum_{\mathbf{k}, \nu, \sigma'} n_{\mathbf{k}\nu\sigma'} \frac{\varepsilon_{\mathbf{k}}^2 x_{\eta\sigma'} x_{-\eta\sigma'}^2}{\varepsilon_{\mathbf{k}\nu\sigma'} y_{\eta\sigma'} y_{-\eta\sigma'}} \\ & \times \left\{ \frac{d_{\eta} [\delta - \xi_{\eta} \Delta n + d_{\eta}^2]^{1/2} - p_{\eta\uparrow} p_{\eta\downarrow}}{p_{\eta\sigma} [\delta - \xi_{\eta} \Delta n + d_{\eta}^2]^{1/2}} \delta_{\sigma, -\sigma'} \right. \\ & + \left[\frac{x_{\eta\sigma}}{y_{\eta\sigma}} \{ \xi_{\eta} \Delta n + \sigma (m + \xi_{\eta} \Delta m) - \delta \} \right. \\ & + \left. \left. \frac{\delta - \xi_{\eta} \Delta n + d_{\eta}^2 - p_{\eta\sigma}^2}{p_{\eta\sigma} [\delta - \xi_{\eta} \Delta n + d_{\eta}^2]^{1/2}} \right] \delta_{\sigma, \sigma'} \right\} \\ & + 4V(1 - \delta - \xi_{\eta} \Delta n), \end{aligned} \quad (22)$$

where the abbreviations

$$x_{\eta\sigma} = [\delta - \xi_{\eta} \Delta n + d_{\eta}^2]^{1/2} p_{\eta\sigma} + p_{\eta-\sigma} d_{\eta}, \quad (23)$$

$$y_{\eta\sigma} = \frac{1}{4} [1 - \{ \delta - \xi_{\eta} \Delta n - \sigma (m + \xi_{\eta} \Delta m) \}^2], \quad (24)$$

as well as the conventions $\xi_{\eta} = 1 (-1) \Leftrightarrow \eta = A (B)$ and $\sigma = 1 (-1) \Leftrightarrow \sigma = \uparrow (\downarrow)$ are used. Notice that for the Peierls gap parameter Δ the relation

$$\frac{\partial f}{\partial \Delta} = 0 \Rightarrow \Delta = 8 \lambda \Delta n \quad (25)$$

holds. Working at fixed n , λ , U , and V the remaining self-consistency loop is given by (16)–(25). Finally, the physically relevant saddle-point is determined to give the lowest free energy (15). Let us emphasize, that our numerical procedure allows for the investigation of metastable solutions.

III. Numerical results

A. The phase diagram of the extended Hubbard model

1. *The $\delta = 0$ case.* We start the numerical evaluation of the SB saddle-point equations at $T = 0$ by analysing the ground state properties of the EHM (i.e. $\lambda, \Delta \equiv 0$). At half-filling ($\delta = 0$), the unperturbed $2D$ tight-binding band structure $\varepsilon_{\mathbf{k}}$ gives rise to perfect (π, π) Fermi surface nesting, leading for $U, V > 0$ to a CDW or SDW instability at the same wave vector.

Comparing the free energies of several symmetry broken states, we obtain the phase diagram of the $2D$ EHM presented in Fig. 1. In the plane of U and V , the phase boundaries are indicated by full lines. Let us first discuss the repulsive case with $U, V > 0$. The physics in this

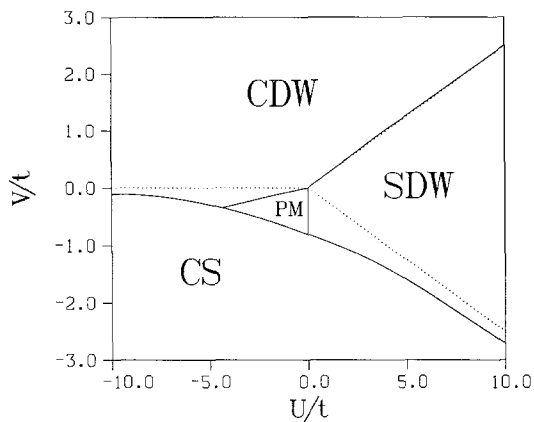


Fig. 1. Slave-boson phase diagram of the 2D extended Hubbard model in the half-filled band sector. The dotted lines show the results of asymptotic expansions (see text)

region is dominated by the competition between U and V , which favours SDW and CDW states, respectively. The SB phase boundary between CDW and SDW (AFM) states is slightly shifted from the Hartree-Fock [18] and 1D renormalisation group [10, 17] result $U = zV$. Here z denotes the number of NN sites. Obviously, this is an effect of the Coulomb correlations which are included in SB mean field treatment. The deviation from the line $U = zV$ was indicated by Lanczos [12, 16] and Monte-Carlo [13, 15, 19] calculations as well. Using the approach of local ansatz [46], Oleś et al. [47] found a qualitatively similar behaviour. The shift of the transition line towards the CDW phase is somewhat smaller than the Lanczos result obtained by Waas et al. [12] for finite chains up to eight sites. At this point it should be mentioned, that our local mean field approximation contains the dimensionality of the problem only via the unperturbed density of states. A comparison with the 2D Monte-Carlo data of Zhang and Callaway [19] yields, e.g., at $U = 4$: $V_{\text{CDW} \rightarrow \text{SDW}} \cong 1.02$ (Fig. 1) and $V_{\text{CDW} \rightarrow \text{SDW}} \cong 1.05$ [19]. We next consider the region where U or V becomes negative. The magnetic susceptibility is evidently suppressed by an attractive interaction [20]. Unfortunately, the SB scheme presented in Sect. II does not contain superconducting correlations which may be of importance in this regime [15, 20] (cf. the discussion in Sect. I). Restricting us to the normal state, we obtain four different phases. Besides CDW and SDW order, the phase diagram exhibits at $U \leq 0$ and $V < 0$ (but $|V|$ not too large) a metallic paramagnetic phase. It is interesting to note that the CDW and SDW correlation functions obtained in this parameter regime from finite-lattice Lanczos calculations have the same order of magnitude. At the same time, the kinetic part of ground state energy becomes strongly enhanced [48]. This may be interpreted as a tendency towards metallic behaviour. For large negative V the system shows a transition to an inhomogeneous charge-separated state (CS). The position of the boundary towards complete phase separation agrees well with the Monte-Carlo results of Lin and Hirsch [15]. In the charge-separated state, the equilibrium configuration consists of two

separated regions with different electron densities n_1 and n_2 . To determine the phase boundary, we compare the free energy of several homogeneous states with the free energy of the two phase system performing the usual Maxwell construction. The ground state energy of the CS state can be easily calculated when the charge separation becomes complete (i.e. $n_1 = 0$ and $n_2 = 2$). The free energies of the various homogeneous phases show a concave curvature for all n as function of n in the CS region, indicating the thermodynamic instability of these states. In other words, the inverse isothermal compressibility of the system,

$$\kappa^{-1} = n^2 \frac{\partial^2 f}{\partial n^2}, \quad (26)$$

becomes negative. Equating the free energies of charge separated and SDW (CDW) states in the limit $U, V \rightarrow \infty$ ($|V| \ll 1, U \rightarrow -\infty$), one gets the asymptotic behaviour marked in Fig. 1 by dotted lines. We found that the transitions $\text{SDW} \rightleftharpoons \text{CDW}$ and $\text{SDW}, \text{CDW}, \text{PM} \rightleftharpoons \text{CS}$ are first-order, whereas the transitions $\text{CDW}, \text{SDW} \rightleftharpoons \text{PM}$ are second-order. Our SB treatment yields no evidence for a crossover from a continuous to a first-order $\text{SDW} \rightleftharpoons \text{CDW}$ transition with increasing U and V . The crossover behaviour has been controversially discussed for the 1D systems [9–14].

The variation of CDW and SDW order parameters along characteristic lines in the parameter space is illustrated in Fig. 2 and 3. In Fig. 2 we show Δn as function of V for the $\text{CDW} \rightleftharpoons \text{PM} \rightleftharpoons \text{CS}$ transition ($U = -4, 0$) as well as for the $\text{CDW} \rightleftharpoons \text{SDW} \rightleftharpoons \text{CS}$ transition ($U = 2, 4, 6$). The jump of Δn for $U > 0$ corresponds to an intersection of the free energies of CDW and SDW states, which is an indication of the first-order transition behaviour. Increasing the Hubbard interaction U at constant V , we obtain the expected reduction of Δn , where at $V < 0$ the CDW order parameter goes continuously to zero (cf. Fig. 3a). Note that for $U > 0$, the sublattice magnetisation

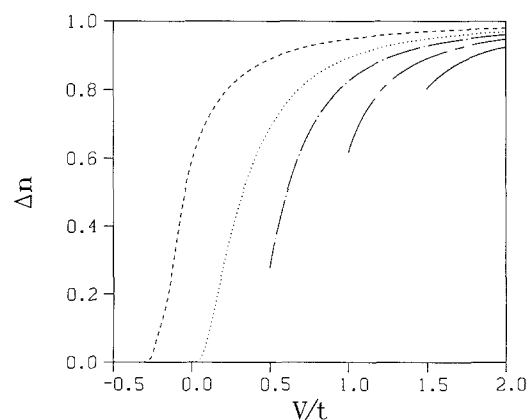


Fig. 2. CDW order parameter Δn as function of the interatomic Coulomb interaction V . The curves are given at various Hubbard interactions $U = -4$ (dashed line), $U = 0$ (dotted), $U = 2$ (chain dotted), $U = 4$ (chain dashed), and $U = 6$ (full)

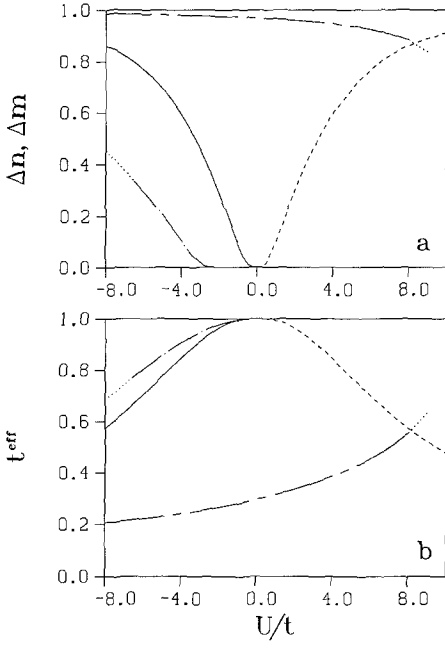


Fig. 3a, b. Order parameters Δn , Δm , and effective hopping amplitude t^{eff} are given as function of U in **a** and **b**, respectively. Δn and t^{eff} are presented in the CDW phase at $V = -0.2$ (chain dotted line), $V = 0$ (full), and $V = 2$ (chain dashed). The dashed curves denotes Δm and t^{eff} in the SDW state, where the results are independent of V . Note that this solution becomes energetically stable only below the CDW \rightleftharpoons SDW transition line. Dotted lines corresponds to a metastable CDW solution

tion is independent of the interatomic Coulomb interaction V . Thus we observe a monotonous increase of Δm with U for the SDW solution even in their instability region. Above (below) the transition point CDW \rightleftharpoons SDW Δn (Δm) breaks down abruptly. In the PM regime both quantities vanish. In order to discuss the mobility of the charge carriers we have calculated the effective transfer amplitude

$$t^{\text{eff}} = \frac{\langle \sum c_{i\sigma}^\dagger c_{j\sigma} \rangle}{\langle \sum c_{i\sigma}^\dagger c_{j\sigma} \rangle_{U, V, \lambda = 0}}. \quad (27)$$

This quantity was used by Lilly et al. [37] to demonstrate the excellent quantitative agreement of SB and quantum Monte-Carlo results for the HM. As can be seen from Fig. 3b, the electronic correlations lead to a reduction of t^{eff} compared to the free electron case. However, it is interesting to notice that t^{eff} becomes enhanced in the PM state and reaches its free electron value even at finite negative V (cf. the chain dotted curve in Fig. 3b). For the repulsive case ($U, V > 0$), t^{eff} exhibits a cusp-structure at the CDW \rightleftharpoons SDW transition point, where the electronic gap is minimal. Due to the large number of double occupied sites on one sublattice, the effective hopping matrix element is reduced in the CDW phase compared to the SDW (AFM) state.

Results showing the renormalized quasiparticle bandwidth versus U for two typical values of the NN inter-

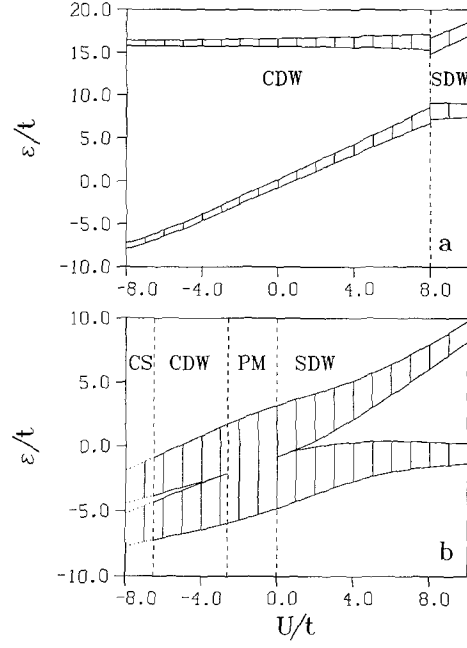


Fig. 4a, b. Renormalized quasiparticle bandwidths in dependence of the intraatomic Coulomb interaction at $V = 2$ **a** and $V = -0.2$ **b**. The corresponding equilibrium states are denoted as in Fig. 1

action ($V > 0$ and $V < 0$) are presented in Fig. 4a and b, respectively. For the CDW and SDW states, the chemical potential μ is situated in the middle of the insulating gap. The band-narrowing with increasing correlations is clearly visible. Note that at the CDW \rightleftharpoons SDW transition, the insulating gap of the SDW state is smaller than the corresponding CDW gap. As a function of U , the position of lower (upper) Hubbard band remains nearly unchanged in the SDW (CDW) phase, whereas the upper (lower) band varies almost linearly with U (see Fig. 4a). This can be understood by performing the well-known attraction-repulsion transformation [49]. For the PM phase the gap disappears and we obtain metallic behaviour. In addition, the local magnetic moment $m_\eta^{\text{loc}} = \frac{3}{4}(n_\eta - 2d_\eta^2)$ takes roughly the value of the band limit, i.e. $m_\eta^{\text{loc}} \simeq 3/8$. m_η^{loc} is a measure for the ‘localisation’ of the electronic spin. In the SDW state m_η^{loc} grows gradually to the atomic limit value $m_\eta^{\text{loc}}(U \rightarrow \infty) = 3/4$.

2. The $\delta \neq 0$ case. The analysis of the ground state properties of the EHM away from half-filling is much more elaborate. In this case, Varma [50] has studied the EHM in the $U < 0, V > 0$ sector by mapping it onto an anisotropic Heisenberg model in the presence of an external field. Alternatively, Laad et al. [51] have performed a canonical transformation onto a field-free $XX-Z$ model at half-filling in the strong coupling limit. Upon doping, they found evidence for singlet superconducting and long-range ordered magnetic phases. However, at least to our knowledge, a more complete study of the phase diagram has not been attempted. To get the SB phase diagram we make use of the saddle-point (16–24) which were derived

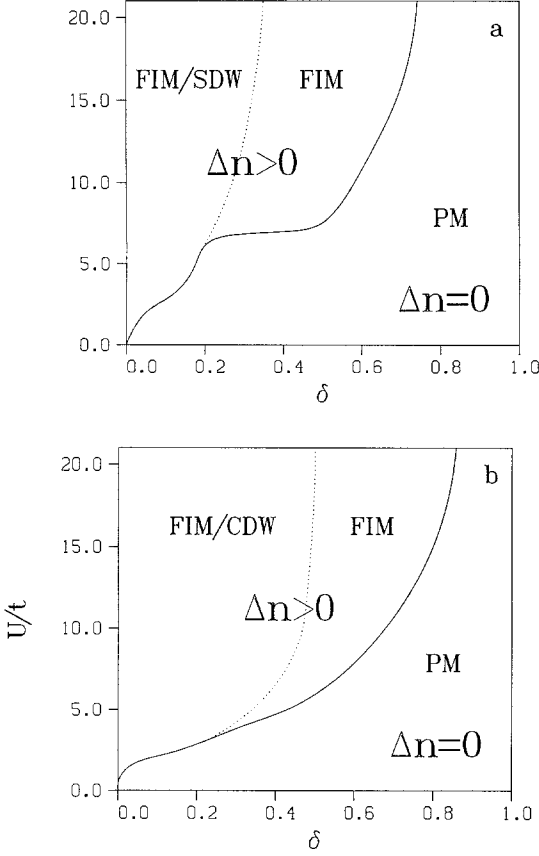


Fig. 5a, b. The domains of stability of several homogeneous phases are depicted for the EHM in the $\delta - U$ plane at $V/U=0.2$ **a** and $V/U=0.3$ **b**. The solid line gives the boundary between states with $\Delta n \neq 0$ and $\Delta n = 0$; the dotted curves separate the various FIM states (cf. the classification in Sect. II)

using only trial states with commensurate structure $[(\pi, \pi)$ or $(0, 0)]$. This is certainly reasonable at half-filling. For the doped case, one cannot exclude other symmetry broken ground states such as incommensurate CDW [52], magnetic textures [53], spiral magnetic order [55, 58], or inhomogeneous phase separated states [29, 30]. However, the incorporation of such states leads to enormous complications in the numerical evaluation of the resulting bosonized action. To keep the problem tractable, we restrict ourselves to states with $A - B$ -sublattice structure even at finite doping, especially in view of the incorporation of an additional electron-phonon coupling in Sect. IIIB.

With this simplification, we first discuss the qualitative features of the phase diagram in the $\delta - U$ plane. Comparing the free energy of different homogeneous phases, we obtain the stability domains presented in Fig. 5. The corresponding variation of the order parameters Δn and Δm are shown in Fig. 6 for a typical value of the Hubbard interaction ($U=10$). The calculations are performed at fixed ratio V/U , where the parameters $V/U=0.2$ (Fig. 5a) and $V/U=0.3$ (Fig. 5b) are chosen to select SDW and CDW states at half-filling. We found that in a large region the doped system exhibits FIM spin order, i.e. the sublattice magnetisations have different magnitudes ($\Delta m \neq 0$).

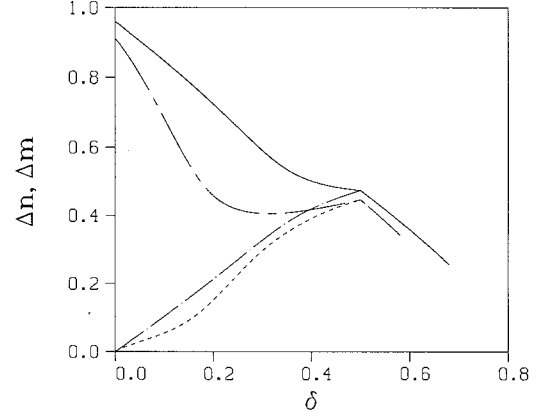


Fig. 6. The doping dependence of Δn (Δm) is given by the full (chain dotted) line at $V/U=0.3$ and by the dashed (chain dashed) curve at $V/U=0.2$

At the same time, however, the CDW order parameter Δn becomes nonzero. Adopting the classification scheme of Sect. II, we distinguish the various FIM states according to the relative importance of SDW and CDW correlations. As can be seen in Fig. 6, the dominance of one or the other order is most pronounced in the vicinity of the half-filled band case. Increasing δ we move into the SDW regime $m_A \gg |m_B|$, where $m_B < 0$ (> 0) for $\delta \leq 0.425$ (≥ 0.425). The resulting net magnetisation obeys the relation $m = (m_A + m_B)/2 = \delta(m = 1 - \delta)$ for $\delta \leq 0.5$ (≥ 0.5). Obviously, there is some arbitrariness in the determination of the FIM/SDW \rightleftharpoons FIM (FIM/CDW \rightleftharpoons FIM) boundary. In the FIM state both types of correlations coexist with the same order of magnitude. For $\delta \geq 0.5$ we have $\Delta n = \Delta m$ until the transition to the paramagnetic phase takes place. Let us emphasize, that the quarter-filled case ($\delta = 0.5$) allows for a commensurate spin and charge structure as well. In fact, we get for the partial occupation numbers:

$$d_\eta^2 = p_{\eta\downarrow}^2 = 0, \quad p_{A\uparrow}^2 \gg p_{B\uparrow}^2 \geq 0, \quad p_{A\uparrow}^2 = e_B^2, \\ \text{and} \quad p_{B\uparrow}^2 = e_A^2.$$

Figure 7 displays the quasiparticle bandwidth of spin up (a) and spin down (b) electrons in the SDW-like state. Note that the bandwidth is strongly renormalized by the electron-electron interaction and has to be self-consistently determined at a given doping level. Below the FIM/SDW \rightleftharpoons PM transition the subbands show spin polarization according to the FIM order. Increasing δ , i.e. lowering the electron density of the system, the electronic correlations become less important and as a result the effective bandwidth is enlarged. The chemical potential (dotted curve) exhibits an anomalous slope near half-filling leading to a negative compressibility ($\kappa^{-1} = -n^2 \partial \mu / \partial \delta$, cf. (3.2)). Adapting the Maxwell construction to the function $\mu(\delta)$, a mixed state with lower free energy can be constructed. Mean field SB approaches to the $t - J$ [56, 57], HM [55, 54, 58] and HPM [29, 30] yield negative compressibility in certain parameter regions. The inclusion of incommensurate spiral states does not pre-

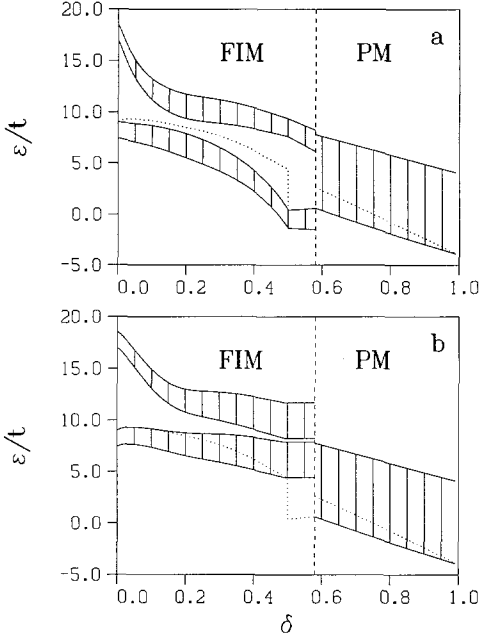


Fig. 7a, b. The location of the quasiparticle bands for spin up **a** and spin down **b** electrons at given hole concentration δ , where $U=10$ and $V/U=0.2$. The dotted line indicates the position of the chemical potential

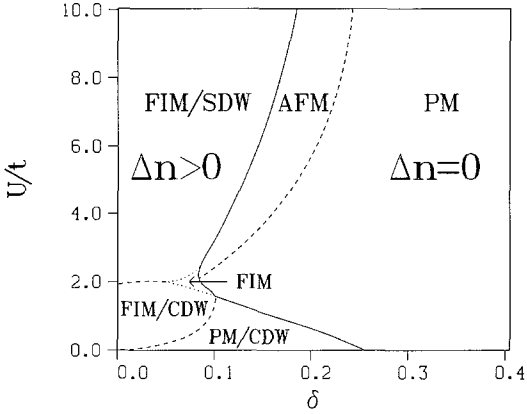


Fig. 8. The phase diagram of the EHM in the $\delta - U$ plane at fixed $V=0.5$

vent the occurrence of this thermodynamic instability [55, 58]. Lanczos diagonalisation studies have found indications of phase separation for the $t - J$ model at large J [8, 59, 60]. Several authors have suggested that the incorporation of long-range Coulomb interactions would suppress such a phase separation on a macroscopic scale [8, 30, 54–59]. Actually, in the SDW domain our results indicate only a weak tendency towards phase separation compared with the findings for the pure HM. For this case the critical doping value δ_c , where κ diverges, is shifted to smaller values. It is interesting to notice, that for the CDW-like state (especially at $V/U > 0.5$) the effect of V is to *enhance* the concave curvature of the free energy, so that the formation of a phase separated ground state is even more favoured.

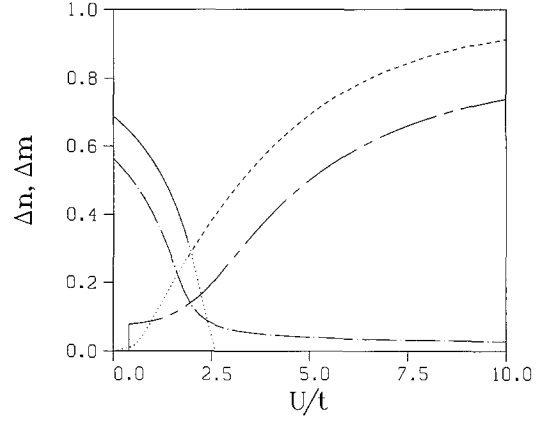


Fig. 9. The variation of the order parameters Δn and Δm with U at $V=0.5$. The full (dashed) line shows Δn (Δm) at half-filling; the chain dotted (chain dashed) curve denotes the results at doping level $\delta=0.075$. Dotted lines denote metastable solutions

To illustrate the crossover from the FIM/CDW to the FIM/SDW solution with increasing U at finite δ , we have calculated the phase diagram of the EHM in the $\delta - U$ plane for fixed $V=0.5$. The result is presented in Fig. 8; in addition, the dependencies of Δn and Δm on U are depicted in Fig. 9 at hole concentrations $\delta=0$ and $\delta=0.075$. The phase diagram shows the range of U , where the effect of V is most pronounced. In the strongly correlated case $U \gg V$, the overall features of the phase diagram are quite similar to the results for the pure HM (see Fig. 15 in Sect. III C). The boundary between states with and without CDW order is given by the solid line. Dashed and solid curves indicate first-order phase transition lines. The FIM domain denotes a crossover region between FIM/CDW and FIM/SDW-like order. Here the phase boundaries (dotted curves) are not well-defined (cf. the order parameters in Fig. 9). The variation of Δn and Δm is compared with the half-filled band case. The abrupt change of Δm indicates the onset of magnetic order at the first-order PM/CDW \rightleftharpoons FIM/CDW transition. In contrast, Δn and Δm show a continuous variation crossing the FIM/CDW \rightleftharpoons FIM \rightleftharpoons FIM/SDW regimes.

B. The extended Hubbard model with Peierls coupling

To discuss the interplay of electron-electron repulsion and electron-lattice interaction we investigate the extended Hubbard-Peierls model in this section. Lattice instabilities due to a static Peierls distortion were studied for the 2D half-filled Hubbard model using both exact diagonalisation methods and perturbation techniques for the large U -limit [61, 62], where the electron-phonon coupling was assumed to affect the hopping matrix element by an additional term proportional to the lattice displacement. It was shown that a critical electron-phonon strength is required to form a so-called ‘dimerized’ state. Furthermore, the frozen in (π, π) phonon mode is found to be the most favourable one at not too large Hubbard interactions U [61]. Using an unrestricted Hartree-Fock approximation, Yonemitsu et al. [63] have shown the

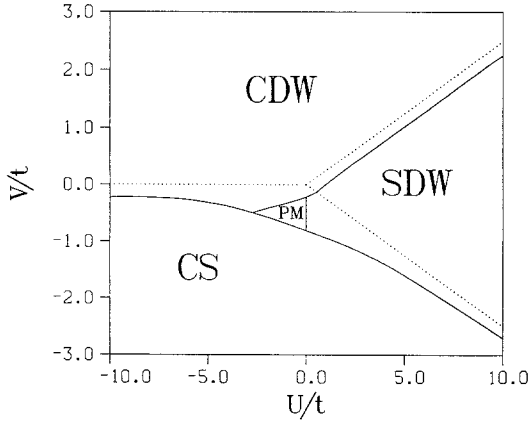


Fig. 10. The SB phase diagram of the 2D extended Hubbard-Peierls model at half-filling. The electron-phonon coupling strength takes the value $\lambda = 0.125$

existence of a CDW state below a critical ratio U/λ for the three-band HPM. The tendency towards ‘dimerization’ was observed for a local Holstein coupling, i.e. the HPM, as well [29, 30, 64] (cf. Sect. IIIC). Here we are concerned with the competing effect of λ and V on the one hand and U on the other hand. To map out the ground state phase diagram of the EHPM, we examine the SB self-consistency loop derived in Sect. II, by taking the additional extremal condition (25) into account.

Starting at half-filling, the $V-U$ phase diagram is shown at fixed electron-phonon coupling $\lambda = 0.125$ in Fig. 10. Compared with the results of Fig. 1 ($\lambda = 0$ case) we found an enlarged region with CDW order. Note that the CDW ordered state is now accompanied by a static (π, π) lattice distortion. These distortions alternately enhance/suppress the effective on-site potentials in our model. According to the lowered (raised) site energies on the A (B)-sublattice one has $d_A^2 = e_B^2 \gg d_B^2 = e_A^2$, where $\Delta n(\lambda, U, V) > \Delta n(0, U, V)$ holds, i.e. an enhancement of the CDW by the local electron-phonon coupling takes place. To show clearly the shift of the CDW \rightleftharpoons SDW, PM, CS transition lines we have marked the asymptotic expansions for the $\lambda = 0$ case as in Fig. 1. In accordance with Monte-Carlo simulations for the 1D model, the CDW \rightleftharpoons SDW phase boundary is slightly displaced from the Hartree-Fock line $4V = U - 8\lambda$ towards the CDW phase. The SDW \rightleftharpoons CS transition is not affected by the Peierls coupling.

In Fig. 11 we present the gap parameter Δ vs U at, e.g., $\lambda = 0.125$. Here we have $\Delta = \Delta n$. Results for other values of λ are qualitatively similar. The abrupt breakdown of the ‘dimerization’ above a critical Coulomb repulsion U_c again illustrates the first-order transition behaviour to the SDW state (the dotted curves belong to metastable solutions). At constant V the gap parameter is a monotonous decreasing function of the Coulomb interaction. Fixing the ratio $V/U = 0.2$, Δ becomes larger, in the ‘dimerized’ (CDW) phase, as U increases. At $U = 0$ the chain dotted line gives the ‘dimerization’ of the simple Peierls model.

In the remainder of this section we analyze our results by doping the system away from half-filling. Viewed as

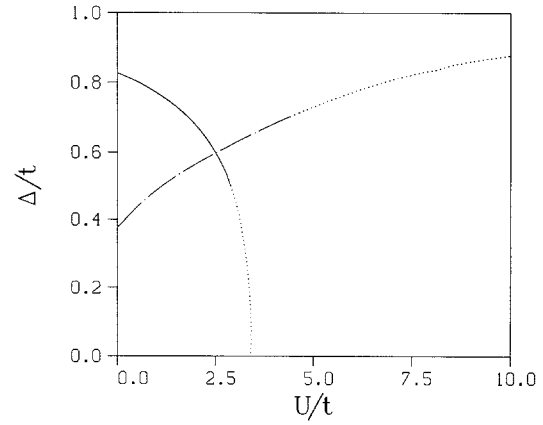


Fig. 11. The Peierls gap parameter Δ is shown as function of Hubbard interaction U for the half-filled EHPM at $\lambda = 0.125$. The stable solution is presented at $V = 0.5$ (full line) as well as at the constant ratio $V/U = 0.2$ (chain dotted line)

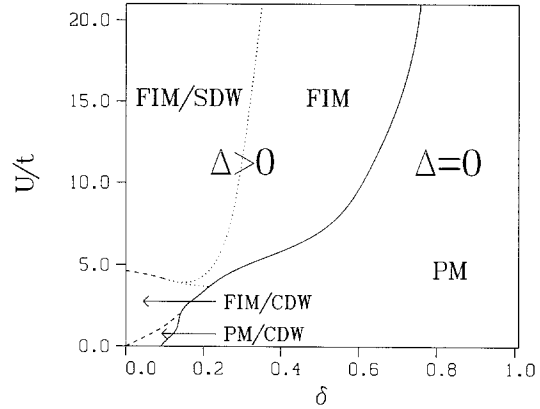


Fig. 12. The phase diagram of the EHPM is calculated in the $\delta - U$ plane for a constant ratio $V/U = 0.2$ at $\lambda = 0.125$

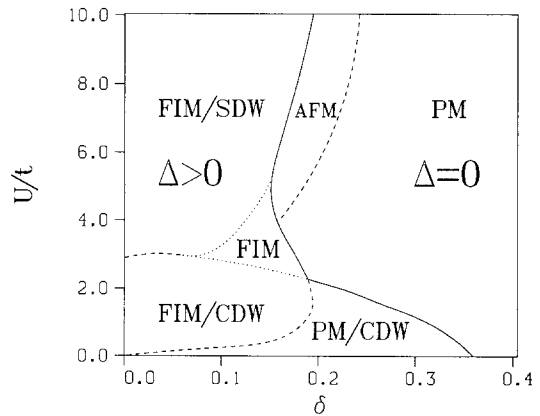


Fig. 13. Phase diagram of the EHPM at $V = 0.5$ and $\lambda = 0.125$

a function of hole concentration, the phase diagrams of the EHPM are displayed at $\lambda = 0.125$ for fixed ratio V/U and for constant V in Figs. 12 and 13, respectively. The most important feature of both phase diagrams is the fact, that for $\delta \neq 0$, there always exists a regime with finite Peierls distortion ($\Delta = 8\lambda\Delta n > 0$), i.e. independent

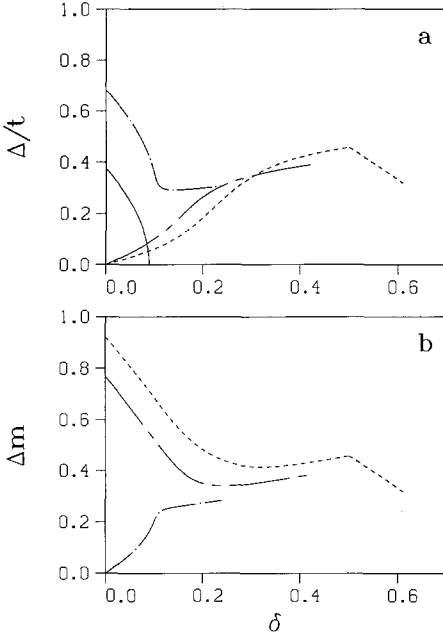


Fig. 14a, b. Gap parameter Δ **a** and order parameter Δm **b** as function of doping δ at $V/U=0.2$ and $\lambda=0.125$. The results are given at $U=0$ (full line), $U=4$ (chain dotted), $U=6$ (chain dashed), and $U=10$ (dashed)

of the intraatomic Coulomb interaction strength. In the limit of large U , the influence of the electron-phonon coupling becomes less important and the phase boundaries of EHM and EHPM merge (cf. Figs. 5a and 12 as well as Figs. 8 and 13, respectively). At the same time the relation $\Delta m \gg \Delta n$ holds in the FIM/SDW state. For small values of the coupling, $U < U_c^{\text{HF}} = 4V + 8\lambda$, the electron-phonon interaction leads to a considerable energy gain due to ‘dimerization’. This tendency becomes stronger reducing U . As a result we found FIM/CDW and PM/CDW states to be lowest in energy. In Figs. 12 and 13, first-order phase boundaries are indicated by full or dashed lines, whereas the dotted curves again denote the FIM/CDW \rightleftharpoons FIM \rightleftharpoons FIM/SDW crossover. Here ‘dimerized’ and ‘undimerized’ phases are separated by full curves.

The doping dependence of Δ and Δm are shown for several values of U in Fig. 14a and b, respectively. In the PM/CDW and FIM/CDW region ($U < U_c^{\text{HF}}$), we found a decrease of the ‘dimerization’ with increasing δ . Doping the system leaves e_B^2 nearly unchanged, whereas the number of doubly occupied sites on the A -sublattice is strongly reduced $d_A^2 < e_B^2$. As a consequence, Δm grows smoothly from zero (if $U > 0$). In the FIM/SDW regime ($U > U_c^{\text{HF}}$), one observes the opposite behaviour. Note that, for small doping concentration ($\delta \ll 1$), the system is in the vacancy regime, i.e. the effective hopping amplitude t^{eff} is still suppressed. At larger doping level, the transition to the FIM state becomes apparent in the $\Delta(\delta)$ and $\Delta m(\delta)$ curves. The cusp structure of both quantities at $\delta=0.5$ is connected to the formation of a commensurate FIM state.

C. Special cases: The Hubbard (-Peierls) model

For completeness, we have studied the HPM and the pure HM at all doping fractions. The SB mean field phase diagram of the HM is shown in Fig. 15. To be consistent with the preceding sections, we have performed numerical calculations for the homogeneous AFM, FM, FIM, and PM phase using the 2D tight-binding density of states. Our results can be compared with the original SB phase diagram of Kotliar and Ruckenstein [35], the $D=\infty$ Gutzwiller phase diagram of Fazekas et al. [65], and a previous study of the present authors [30]. However, these investigations take only AFM, FM, and PM phases into account. One of the most interesting results is that the inclusion of FIM states changes the phase diagram considerably. Away from half-filling the FIM state becomes energetically more favourable than the AFM one in a large parameter region. FIM solutions at finite doping has been found by Oleś [66] using a variational ground state according to the local ansatz [46]. By contrast, the region of their so-called ‘special ferromagnetic state’ [66] is much broader than that of the FIM slave-boson solution. It is worthwhile to note that our FIM state has, in the sense of Sect. II, SDW character. Going away from half-filling, the order parameter Δm decreases monotonously from its maximum AFM-value at $\delta=0$. On the other hand, the CDW order parameter Δn increases from zero with increasing hole concentration δ (but is still one order of magnitude smaller than Δm). This can be mainly attributed to a reduction of doubly occupied sites on one sublattice. Again $m=\delta$ holds. Therefore, we can conclude that, within the limitations of our calculations, even the positive- U Hubbard model shows a tendency towards weak CDW order for $\delta \neq 0$. In the limit $U \rightarrow \infty$ the FM region extends from $\delta=0^+$ to $\delta_{\text{FM}=\text{PM}}=0.33$. At $U=\infty$, the FM free energy exhibits convex curvature independent of the doping level. Thus, the SB theory does not support the arguments for phase separation in this limit [67]. A phase diagram, including mixed phases at finite U , was recently presented in [30]. To improve the calculations further, it would be interesting to incorporate incommensurate SDW/CDW states [55, 58] as well as magnetic short range order effects [68].

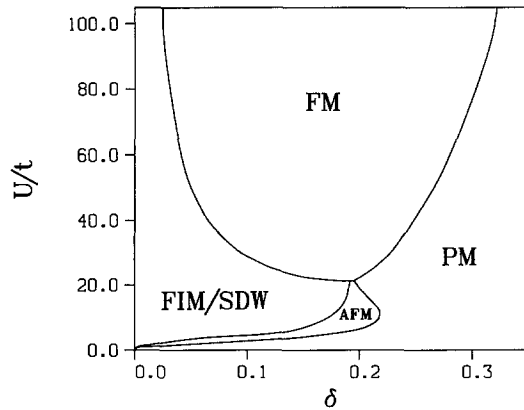


Fig. 15. The restricted SB phase diagram of the 2D Hubbard model contains homogeneous PM, FM, FIM/SDW, and AFM states. At $\delta=0$ we get an AFM ground state

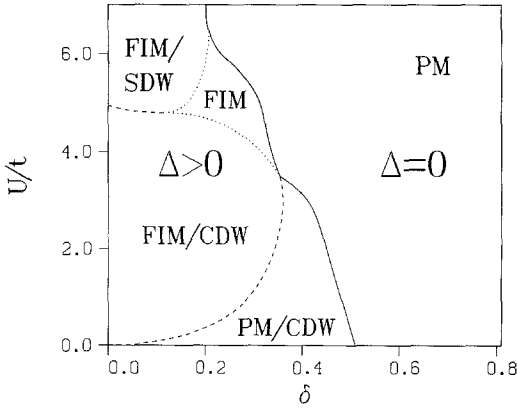


Fig. 16. Phase diagram of the 2D Hubbard-Peierls model at $\lambda=0.625$. The solid line separates ‘dimerized’ from ‘undimerized’ states

Finally, we show the corresponding ground state phase diagram of the Hubbard-Peierls model in Fig. 16. Obviously, the ‘dimerized’ solutions are lowest in energy for a large parameter region of U and δ . A finite gap parameter is related to CDW order ($\Delta = 8\lambda\Delta n$). Thus the electron-phonon coupling enhances the CDW order parameter of the pure HM ($\Delta n(\lambda, U) > \Delta n(0, U)$) and, of course, $\Delta(\lambda, U) > \Delta(0, U) \equiv 0$. The effect becomes strongest at half-filling, where $\Delta n(\lambda, U) \geq 0$ for $U \leq U_c(\lambda)$ but $\Delta n(0, U) \equiv 0$. The dashed phase boundary between FIM/CDW and FIM/SDW denotes a first-order transition connected to a jump of Δm and Δ , whereas both quantities vary continuously along the FIM/CDW \rightleftharpoons FIM \rightleftharpoons FIM/SDW transition line. Let us emphasize that the inclusion of the FIM/SDW state with finite Δn enlarges the ‘dimerized’ region ($\Delta \neq 0$) considerably. For comparison we refer to the phase diagram, given by the authors in a previous paper [29], where only the FIM/CDW state was taken into account.

IV. Concluding remarks

In this paper we have applied the slave-boson mean field approach, first introduced by Kotliar and Ruckenstein [35], to the 2D (extended) Hubbard-(Peierls) models. The SB scheme enables us to treat electron-electron as well as electron-phonon interaction over the whole range of coupling strength on an equal footing. From our extensive numerical evaluation of the resulting two-sublattice self-consistency equations, we believe we get some insight into the main features of the ground state phase diagrams of the HM, HPM, EHM, and EHPM. The phase diagrams are obtained by comparing the free energy of appropriate symmetry broken states (cf. the classification in Sect. II) as a function of band filling and interaction strengths. Our main results for the different models are summarized as follows:

(i) The SB phase diagram of the EHM at $\delta = 0$ is in good agreement with previous Monte-Carlo and Lanczos results. The CDW \rightleftharpoons SDW transition is shifted from the

mean-field line towards the CDW region. Besides CDW and SDW phases, we found at $V < 0$ evidence for a PM regime. For large negative V , the electrons undergo a condensation transition to a charge separated state (CS). Off half-filling, the phase diagram becomes more complex: we observe PM/CDW, FIM/CDW, FIM/SDW, FIM, AFM, and PM regions. The effective bandwidth is strongly renormalised by electronic correlations. The interatomic Coulomb interaction suppresses (enhances) the tendency towards phase separation in the SDW (CDW) regime.

(ii) Incorporating the local electron-phonon coupling, the tendency towards CDW order is enhanced. Whereas the SDW \rightleftharpoons CS transition is not affected by the Peierls coupling, the CDW \rightleftharpoons SDW, PM, CS phase boundaries are displaced. The CDW phase is accompanied by a static (π, π) Peierls distortion, where the solution with finite ‘dimerization’ gives the lowest free energy in a considerable parameter regime of U , V , and δ . Increasing the Hubbard interaction U , at $\delta = 0$, the ‘dimerization’ decreases (increases) for fixed V (V/U) in the CDW state. The transition to the undimerized state is first-order. Away from half-filling, there is a transition between FIM/CDW ($\Delta \gg \Delta m$) and FIM/SDW ($\Delta m \gg \Delta$) at $U \simeq 4V + 8\lambda$. For the quarter-filled band, we found a commensurate FIM state, where $\Delta n = \Delta m$.

(iii) The two-sublattice SB phase diagram of the Hubbard model contains AFM, FM, PM and FIM/SDW states. Upon doping, the FIM/SDW phase becomes energetically more favourable than the AFM one in a large region. Note that the FIM/SDW solution shows weak CDW order, i.e. $\Delta n \neq 0$ (but $\Delta m \gg \Delta n$).

(iv) In the Hubbard-Peierls model, this tendency is enhanced due to the additional electron-phonon interaction. Actually, this is similar to the results for the EHPM. Let us emphasize, that even the FIM/SDW state exhibits a finite lattice distortion.

It would be very interesting to investigate the $t - J$ -Peierls model in an analogous way. Whereas the physics of the HPM model near half-filling is dominated by the Peierls instability, this type of CDW instability is suppressed in the $t - J$ -Peierls model. Therefore, local (rather than global) lattice distortions, such as small hole-polarons, gain in importance [25, 32]. To treat these problems within the SB scheme, one has to go beyond the two-sublattice mean-field approximation. Work along this line, also including nonadiabatic effects due to a finite phonon frequency, is in progress.

We would like to thank D. Ihle, A. Muramatsu, U. Trapper and V. Waas for helpful discussions.

References

1. Anderson, P.W.: Science **235**, 1196 (1987)
2. See, for example: Strongly correlated electron systems, Vol. I, II, III, Baskaran, G., Ruckenstein, A.E., Tosatti, E., Lu, Y. (eds.). Singapore: World Scientific 1990, 1991, 1992
3. Balachandran, A.P., Ercolessi, E., Morandi, G., Srivastava, A.M.: Hubbard model and anyon superconductivity. Singapore: World Scientific 1990

4. Moriya, T.: Spin fluctuations in itinerant electron magnetism. Berlin, Heidelberg, New York: Springer 1985
5. Mott, N.F.: Metal-insulator transitions. London: Taylor and Francis 1990
6. Campell, K., DeGrand, T.A., Mazumdar, S.: Phys. Rev. Lett. **52**, 1717 (1984)
7. Schulz, H.J.: Phys. Rev. Lett. **64**, 2831 (1990)
8. Emery, V.J., Kivelson, S.A., Lin, H.Q.: Phys. Rev. Lett. **64**, 475 (1990)
9. Fourcade, B., Spronken, G.: Phys. Rev. **B29**, 5089 (1984); Phys. Rev. **B29**, 5094 (1984)
10. Voit, J.: Phys. Rev. **B45**, 4027 (1992)
11. del Bosch, L.M., Falicov, L.M.: Phys. Rev. **B37**, 6073 (1988)
12. Waas, V., Büttner, H., Voit, J.: Phys. Rev. **B41**, 9366 (1990)
13. Cannon, J.W., Scalettar, R.T., Fradkin, E.: Phys. Rev. **B44**, 5995 (1991)
14. Hirsch, J.E.: Phys. Rev. Lett. **53**, 2327 (1984)
15. Lin, H.Q., Hirsch, J.E.: Phys. Rev. **B33**, 8155 (1986)
16. Cannon, J.W., Fradkin, E.: Phys. Rev. **B41**, 9435 (1990)
17. Emery, V.J.: Highly conducting one-dimensional solids, p. 247. Devreese, J.T., Evrard, R.P., van Doren, V.E. (eds.). New York: Plenum 1979
18. Cabib, D., Callen, E.: Phys. Rev. **B12**, 5249 (1975)
19. Zhang, Y., Callaway, J.: Phys. Rev. **B39**, 9397 (1989)
20. Micnas, R., Ranninger, J., Robaszkiewicz, S.: Rev. Mod. Phys. **62**, 113 (1990)
21. Alexandrov, A.S., Ranninger, J.: Phys. Rev. **B23**, 1796 (1981)
22. Tsuda, N., Nasu, K., Yanese, A., Siratori, K.: Electronic conduction in oxides. Berlin, Heidelberg, New York: Springer 1990
23. Holstein, T.: Ann. Phys. **8**, 343 (1959)
24. Prelovšek, P., Rice, T.M., Zhang, F.C.: J. Phys. **C20**, L229 (1987); Prêtre, A., Rice, T.M.: J. Phys. **C19**, 1365 (1986)
25. Muramatsu, A., Hanke, W.: Physica **C135**, 229 (1988)
26. Zheng, H., Feinberg, D., Avignon, M.: Phys. Rev. **B41**, 11557 (1990)
27. Nasu, K.: Phys. Rev. **B44**, 7625 (1991)
28. Kim, J.H., Levin, K., Wentzcovitch, R., Auerbach, A.: Phys. Rev. **B44**, 5148 (1991)
29. Fehske, H., Deeg, M., Büttner, H.: Phys. Rev. **B46**, 3713 (1992)
30. Deeg, M., Fehske, H., Büttner, H.: Z. Phys. **B88**, 283 (1992)
31. Das, A.N., Konior, J., Ray, D.K., Oleś, A.M.: Phys. Rev. **B44**, 7680 (1991)
32. Röder, H., Fehske, H., Büttner, H.: Phys. Rev. B (accepted for publication) (1993)
33. Chakraverty, B.K., Feinberg, D., Zheng, H., Avignon, M.: Solid State Commun. **64**, 1147 (1988); Alexandrov, A.S.: Phys. Rev. **B38**, 925 (1988) Ranninger, J.: Z. Phys. **84**, 1147 (1991)
34. Chakraverty, B.: J. Phys. (Paris) **42**, 1351 (1981)
35. Kotliar, G., Ruckenstein, A.E.: Phys. Rev. Lett. **57**, 1362 (1986)
36. Schmeltzer, D., Bishop, A.R.: Europhys. Lett. **12**, 369 (1990)
37. Lilly, L., Muramatsu, A., Hanke, W.: Phys. Rev. Lett. **65**, 1379 (1990)
38. Frésard, R., Wölfle, P.: Int. J. Mod. Phys. **B6**, 685 (1992)
39. Barnes, S.E.: J. Phys. **F6**, 1375 (1976)
40. Read, N., Newns, D.M.: J. Phys. **C16**, L1055 (1983)
41. Coleman, P.: Phys. Rev. **B35**, 5072 (1987)
42. Li, T., Wölfle, P., Hirschfeld, P.J.: Phys. Rev. **B40**, 6817 (1989)
43. Popov, V.N.: Functional integrals in quantum field theory and statistical physics. Cambridge: Cambridge University Press 1987
44. Hooijer, G., Van Himbergen, J.E.: Phys. Rev. **B36**, 7678 (1987)
45. Jolicoeur, T., Le Guillou, J.C.: Phys. Rev. **B44**, 2403 (1991)
46. Stollhoff, G., Fulde, P.: Z. Phys. **B26**, 257 (1977)
47. Oleś, A.M., Micnas, R., Robaszkiewicz, S., Chao, K.A.: Phys. Lett. **102A**, 323 (1984)
48. Waas, V.: private communication
49. Shiba, H.: Prog. Theor. Phys. **48**, 2171 (1972)
50. Varma, C.M.: Phys. Rev. Lett. **61**, 2713 (1988)
51. Laad, M.S., Ghosh, D.K.: J. Phys. **C3**, 9723 (1991)
52. Batistić, L., Gammel, J.T., Bishop, A.R.: Phys. Rev. **B44**, 13228 (1991)
53. Bishop, A.R., Guinea, F., Lomdahl, P.S., Louis, E., Vergés, J.A.: Europhys. Lett. **14**, 157 (1991)
54. Frésard, R., Wölfle, P.: preprint (1991)
55. Arrigoni, E., Strinati, G.C.: Phys. Rev. **B44**, 7455 (1991)
56. Uchinami, M.: Phys. Rev. **B42**, 10178 (1990)
57. Ivanov, T.I.: Phys. Rev. **B44**, 12077 (1991)
58. Frésard, R., Dzierzawa, M., Wölfle, P.: Europhys. Lett. **15**, 325 (1991)
59. Fehske, H., Waas, V., Röder, H., Büttner, H.: Solid State Commun. **76**, 1333 (1990); Fehske, H., Waas, V., Röder, H., Büttner, H.: Phys. Rev. **B44**, 8473 (1991); Röder, H., Fehske, H., Waas, V., Büttner, H.: Phys. Rev. **B45**, 13092 (1992)
60. Moreo, A., Scalapino, D., Dagotto, E.: Phys. Rev. **B43**, 11442 (1991)
61. Tang, S., Hirsch, J.E.: Phys. Rev. **B37**, 9546 (1988)
62. Zhang, F.C., Prelovšek, P.: Phys. Rev. **B37**, 1569 (1988)
63. Yonemitsu, K., Bishop, A.R., Lorenzana, J.: preprint (1992)
64. Hirsch, J.E.: Phys. Rev. **B31**, 6022 (1985)
65. Fazekas, P., Menge, B., Müller-Hartmann, E.: Z. Phys. **B78**, 69 (1990)
66. Oleś, A.M.: J. Phys. **C15**, L1065 (1982)
67. Visscher, P.B.: Phys. Rev. **B10**, 943 (1974)
68. Zhang, W., Avignon, M., Bennemann, K.H.: Phys. Rev. **B45**, 12478 (1992)